NANOMATERIALS SCIENCE & ENGINEERING
Vol. 4, No. 1, pp. 10-20 (2022)

RESEARCH ARTICLE

https://doi.org/10.34624/nmse.v4i1.29956

Tunnel magnetoresistance of granular superparamagnetic and ferrimagnetic structures

Gunnar Suchaneck

Institute of Solid-State Electronics, TU Dresden, 01062 Dresden, Germany
Corresponding author, e-mail address: Suchaneck@tu-dresden.de

Received 1 September 2022; accepted 16 November 2022; published online 20 December 2022

ABSTRACT

Applicable magnetic sensors based on nanogranular ferromagnetic materials were developed already more than 25 years ago. Since the then, nanotechnology has advanced significantly. New methods for manufacturing agglomerated core-shell structures have emerged. This opens up new possibilities of sensor fabrication and an opportunity for reassessment of the electric and magnetic properties of ideal granular structures. This work represents a comprehensive study of the intergranular resistivity, tunnel magnetoresistance and magnetic field sensibility of superparamagnetic and ferro(ferri)magnetic granular materials. Starting with the tunnel resistance of a granular metal network in which the grains are interconnected by insulating barriers, the tunnel magnetoresistance is calculated under consideration of the temperatures dependencies of magnetization, spin polarization and the magnetic flux dependencies of magnetization and tunnelling barrier height. Granular, superparamagnetic materials show a higher magnetic field sensitivity than ferromagnetic ones. They show a lower temperature coefficient of the tunnel magnetoresistance. Owing to their small magnetic response a higher temperature, superparamagnetic ferrimagnetic oxides are not suitable for application at room temperature. Ferromagnetic nanoparticles possess a high field sensitivity only in a small region of 0.1 to 0.5 T.

1. INTRODUCTION

A granular material is a conglomeration of solid particles characterized by a loss of energy whenever the particles interact [1]. A small negative magnetoresistance was observed in granular superparamagnetic (SPM) Ni-SiO_2 thin films of 5-6 nm diameter made by co-sputtering of Ni and SiO_2 already 50 years ago [2]. The appearing magnetoresistance was attributed to tunnelling of spin-polarized electrons between the metallic granules. Its low value is explained by a low spin polarization of Ni amounting to 11 % at low temperatures [3]. Nanogranular, magnetic Fe-B-N thin films were first prepared by cosputtering of Fe-B and BN in 1985 [4]. The films were composed of two amorphous phases of Fe-B and B-N with a size of about 5 nm. They possessed a high specific electrical resistivity ρ in the order of 1-100 mΩ·cm and a saturation magnetization of 2.1 μ_B/at at low temperatures. In 1994, large tunnel magnetoresistance (TMR) of 8 % at 1.2 T and room temperature was obtained in Co-Al-O nanogranular films with a resistivity of about 100 mΩ·cm [5]. These films consist of two phases – SPM, metallic Co granular grains and Al_2O_3 narrow intergrains. Hence, the electrical conductance is governed by tunnelling between Co grains through Al_2O_3 tunnel barriers. Comparable values were reported in the next years for granular Co-Si-O [6], Co-Re-O, Re = Y, Nd, Sm, Gd, Tb, Dy [7], Fe-Al-O [8,9], Fe-Mg-O [10], Fe-Si-O [11,12,13], Fe-Hf-O [14], and Fe-Re-O, Re = Y, Nd, Sm, Gd, Tb, Dy [7]. A TMR of up to 7.5 % at 78 K and 1 T was obtained for granular Fe–MgF_2 thin films [15]. Later in 2001, TMR values up to about 14 % at room temperature and 1 T were observed in a 32 vol%($Fe_{0.51}Co_{0.49}$)–(Mg–F) thin film [16].

Here, the (Mg-F) intergranules were in the crystalline MgF_2 state enabling a higher TMR compared to Co-Al-O film with an amorphous structure of Al-oxide intergranules. Regardless, the proposed applications of nanogranular magnetic films were just noise suppression in the microwave range [17] and magneto-optic devices based on the Faraday effect [18].

The first granular thin films were mainly fabricated by reactive co-sputtering of two metals or co-sputtering of a metal and a dielectric in a way that a two-phase structure was formed. Since the 2000ies, nanotechnology has advanced significantly. New methods for manufacturing agglomerated core-shell structures have emerged. This opens up new possibilities of sensor fabrication and an opportunity for reassessment of the electric and magnetic properties of ideal granular structures.

In this work, the intergranular resistivity, tunnel magnetoresistance and magnetic field sensibility of SPM and ferro(ferri)magnetic (FM) granular materials are examined theoretically. Starting with the tunnel resistance of a granular metal network in which the grains are interconnected by insulating barriers, the tunnel magnetoresistance is calculated under consideration of the temperatures dependencies of magnetization, spin polarization and the magnetic flux dependencies of magnetization and tunnelling barrier height. Both, SPM and FM nanoparticles (NPs) are considered.

2. INTERGRANULAR RESISTIVITY, TUNNEL MAGNETORESISTANCE AND MAGNETIC FIELD SENSIBILITY

2.1. Intergranular resistivity and magneto-resistance caused by spin-polarized tunnelling

The resistivity of a granular metal network in which the metal grains are interconnected by insulating barriers is given by [19]

$$\rho_T(T) \propto \exp\left(f\chi w + \frac{E_c}{2kT} \right), \quad (1)$$

where f is a barrier shape factor, $f = 2$ for rectangular barriers and $f = \pi/2$ for parabolic barriers, χ is the reciprocal localization length of the wave function

$$\chi = \sqrt{\frac{2m^* V_0}{\hbar^2}}, \quad (2)$$

with m^* is the effective electron mass, V_0 the barrier height, $\hbar$ is the reduced Planck constant, w the barrier width, E_c the charging energy of the grains, k the Boltzmann constant, and T the absolute temperature. Note that we are considering thin enough barriers in the order of 1 to 3 nm where direct tunnelling occurs which is not disturbed by localized states in the thin barrier film. An estimation of E_c for grains of diameter d – much larger than the barrier width w – is given by equation [20]

$$E_c \approx \frac{4e^2 w}{\varepsilon\varepsilon_0 d^2}, \quad (3)$$

with ε the dielectric permittivity and ε_0 the vacuum permittivity, respectively. Since the charging energy is reciprocal to the grain diameter, charging effects become significant at small grain sizes.

Tunnelling itself is a temperature-independent transport process [21]. Spin-dependent electron tunnelling depends on the relative orientation of magnetic moments between the ferrimagnetic grains. The tunnel resistance decreases when the magnetic moments of the grains are aligned in parallel in an applied magnetic field. If the angle between the magnetizations on both sides of the tunnelling barrier is randomly distributed between 0 and π, the resistivity given by [22]

$$\rho_T(T) = \frac{\rho_0 \cdot \exp(f\chi w)}{1 + m^2(B,T) \cdot P^2}, \quad (4)$$

with m the relative magnetization, i.e. the magnetization scaled to the saturation magnetization, and P the spin polarization in the magnetic grains.

The temperature dependence of the tunnelling spin polarization can be represented as follows [23]

$$P(T) = P_0(1 - g_P T^{3/2}), \quad (5)$$

where P_0 equals to 0.44, 0.34, 0.85, 0.72 and 0.55 for Fe, Co, $La_{2/3}Sr_{1/3}MnO_3$, $Sr_2FeMoO_{6-\square}$ and Fe_3O_4 respectively, whereas g_P can be estimated using the Curie temperature T_C

$$g_P \approx T_C^{-3/2} \ . \quad (6)$$

Following equation (2), the decay of wavefunction in a barrier material depends on the barrier height. Consequently, we have to consider the barrier height in dependence on the magnetic flux density *B*. The magnetic field dependence of the tunnelling barrier was taken in the form of a series expansion [24]

$$V_0(B) = V_0(0) - \beta B + \gamma B^2 . \quad (7)$$

The coefficient β is attributed in to Zeeman splitting amounting about 1 μ_B, i.e., 0.058 meV/T for a magnetic field perpendicular and about 20 μ_B for a magnetic field applied parallel to the current. The coefficient γ is adapted from data of a magnetic sensor based on a tunnelling device comprising a 2 nm thick double perovskite $La_2Co_{0.8}Mn_{1.2}O_6$ layer grown on top of a Nd-doped $SrTiO_3$ substrate and capped with a thin Pt layer [24].

We have developed a more complex model for the intergranular TMR of strontium ferromolybdate ($Sr_2FeMoO_{6-\delta}$, SFMO) ceramics caused by spin-polarized tunnelling [25]. Taking the resistivity of a granular metal network in which the metal grains are interconnected by insulating barriers, equation (1), and accounting only small changes of the barrier height by the applied magnetic field, this yields a TMR of

$$TMR = \frac{\rho(B)}{\rho(0)} - 1 = \frac{(1+m(0,T)^2 \cdot P^2) \cdot exp\left(f\chi(0) \cdot w \cdot \frac{\delta V_0}{2V_0}\right)}{(1+m(B,T)^2 \cdot P^2)} - 1 \ , \quad (8)$$

where $\rho(B)$ is the resistivity for a given magnetic flux density *B*. For very large barrier heights and very soft magnetic materials we obtain the well-known relation [26]

$$TMR = -\frac{m^2P^2}{1+m^2P^2} = \frac{1}{1+m^2P^2} - 1. \quad (9)$$

In the latter model, the maximum TMR is -50 %.

2.2. Granular networks of noninteracting superparamagnetic nanoparticles

The remanent magnetization of uniaxial, single-domain NPs which are fully magnetized along the easy axis vanishes after removing the magnetic field as

$$M = M_s \exp\left(-\frac{t}{\tau}\right) , \quad (10)$$

where M_s is the saturation magnetization, *t* the time after removal of the field. The value τ denotes the Néel-Brown relaxation time for an energy barrier $\Delta E = KV$ [27,28]

$$\tau = \tau_0 \exp\left(\frac{KV}{kT}\right), \quad (11)$$

with τ_0 a time constant in the order of nanoseconds [29], *K* the uniaxial anisotropy constant, *V* the particle volume. Note that the uniaxial anisotropy constant is also temperature dependent [30].

SPM behavior is obtained using an instrument with a characteristic measuring time τ_m larger than τ. For τ_m less than τ, the magnetic moments remain in a fixed direction during the measurement. This leads to a remanent magnetization and appearance of a coercive field, thus, a metastable FM state is detected. The condition $\tau = \tau_m$ defines the so-called blocking temperature T_B [31]

$$T_B = \frac{KV}{k \cdot \ln(\tau_m / \tau_0)} . \quad (12)$$

Here, the characteristic measuring time amounts to ca. 100 seconds in static magnetometry [32]. Particles above the blocking temperature reveal a dominating SPM behaviour, while particles below the blocking temperature show a predominant FM behaviour. In the latter case thermal excitations are not sufficient to overcome the energetic barrier. The critical size below which SPM behaviour is obtained, d_{cr}^{spm}, then yields

$$d_{cr}^{spm} = \left(\frac{\pi \cdot \ln(\tau_m / \tau_0) \cdot kT}{6 \cdot K(T)}\right)^{1/3} . \quad (13)$$

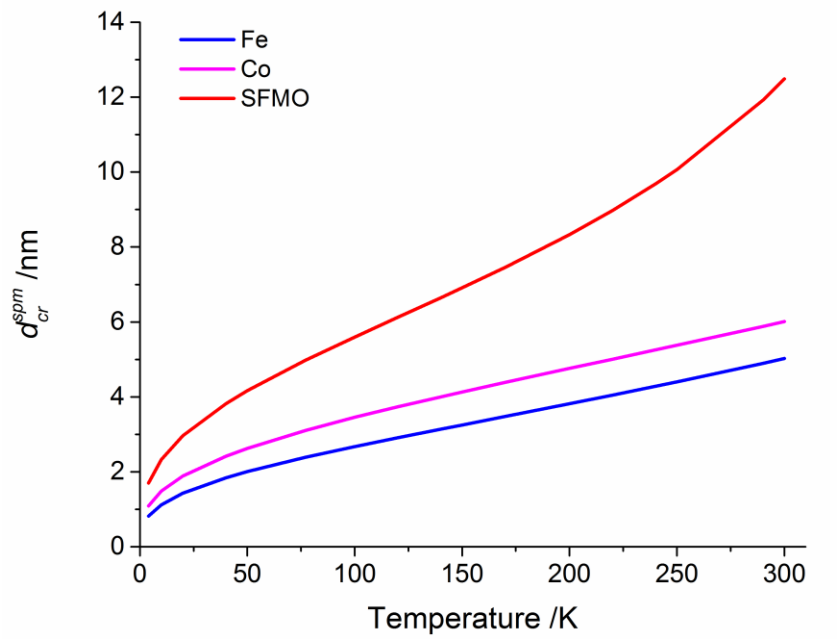

Figure 1. Temperature dependence of the SPM critical diameter, equation (13).

.

Figure 1 shows the temperature dependence of the critical size of Fe, Co and SFMO.

$K(T)$ varies as a function of the reduced temperature T/T_C with T_C the Curie temperature

$$K(T) = K(0)\cdot\left(1-\frac{T}{T_C}\right)^{\eta} . \quad (14)$$

On the other hand, the dependence of the anisotropic constant on magnetization obeys a power law

$$\frac{K(T)}{K(0)} = \left[\frac{M(T)}{M(0)}\right]^{n} , \quad (15)$$

with a coefficient $n = 3$ for uniaxial anisotropy and $n = 10$ for cubic one [33,34]. In the presentation of equation (15), the reduced magnetization has a power coefficient of 1/3

$$m = \frac{M_s(T)}{M_s(0)} = \left(1-\frac{T}{T_C}\right)^{1/3} , \quad (16)$$

which was derived from Monte-Carlo and Landau–Lifshitz–Gilbert simulations [35]. This yields $\eta = 10/3$ and $\eta = 1$ for SFMO. The experimental value of η for core-shell $Sr_2FeMoO_{6-\delta}$-$SrMoO_4$ core-shell structures amounts to $\eta = 4/3$ [36]. At nonideal interfaces, the second-order anisotropy constant comes into play [37] so that in our case the power coefficient becomes $\eta > 1$. A value of $n = 4$ indicates that the second-order anisotropy constant plays a significant, albeit not overwhelming, role.

With regard that the approximations made for the reduced magnetization fail at very low temperatures, we have to deal with particles sizes in the order of 5 to 10 nm. Reducing further the NP size, surface effects become dominant and the ideal model of a giant spin formed by all the spins of the particle pointing in the anisotropy direction and coherently reversing due to thermal activation is no longer valid. For example, fcc Co NPs having about 200 atoms will have diameters around 1.6 nm and 60% of the total spins are located at the surface [38]. Surface spin canting reduces the magnetization yielding strong deviations from the bulk behaviour. This latter size effect is beyond the scope of this paper.

The reduced magnetization of SPM NPs resembles the Langevin behavior of paramagnetic materials [32]

$$m = \frac{M_s(T)}{M_s(0)} = L(\zeta B) = coth(\zeta B) - 1/(\zeta B),\ \zeta = \frac{\mu}{kT} , \quad (17)$$

where μ is the magnetic moment of the NP depending on its size. Note that Eq. (17) is valid only for a noninteracting system [2]. The effects of interactions may be accounted for by adding a mean field to the applied field, i.e., $B=B_a+\mu_0\lambda M$ with B_a the applied magnetic flux and λ an interaction parameter. Figure 2 shows the reduced magnetization of iron NPs with a diameter of 10 nm with the magnetic flux density as a parameter. Note that SPM particles above T_B show no hysteresis. However, since the SPM NP acts as a giant spin, the magnetization and the magnetic susceptibility of a SPM material are much larger compared to that of a paramagnetic material.

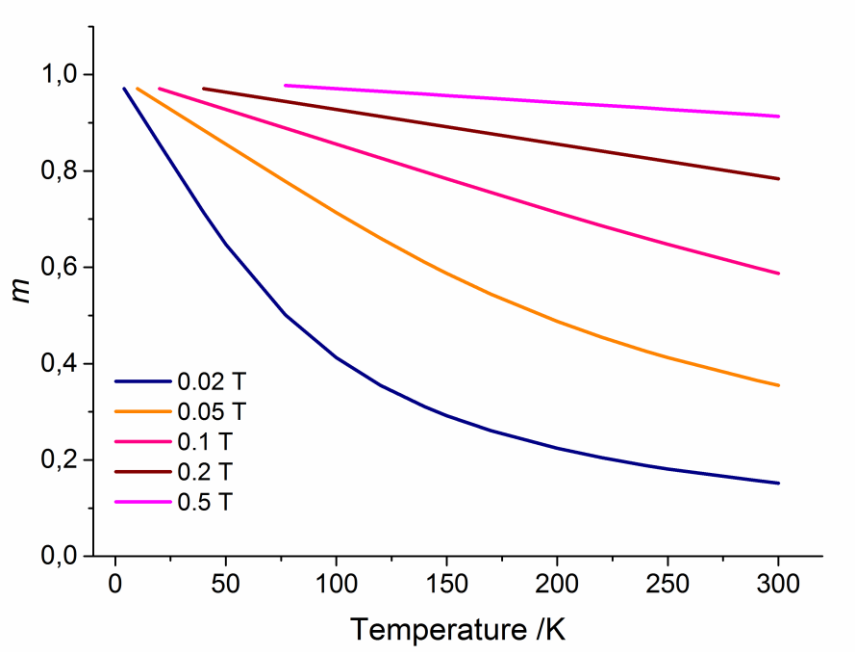

Figure 2. Temperature dependence of the reduced magnetization of Fe NPs with a d = 10 nm.

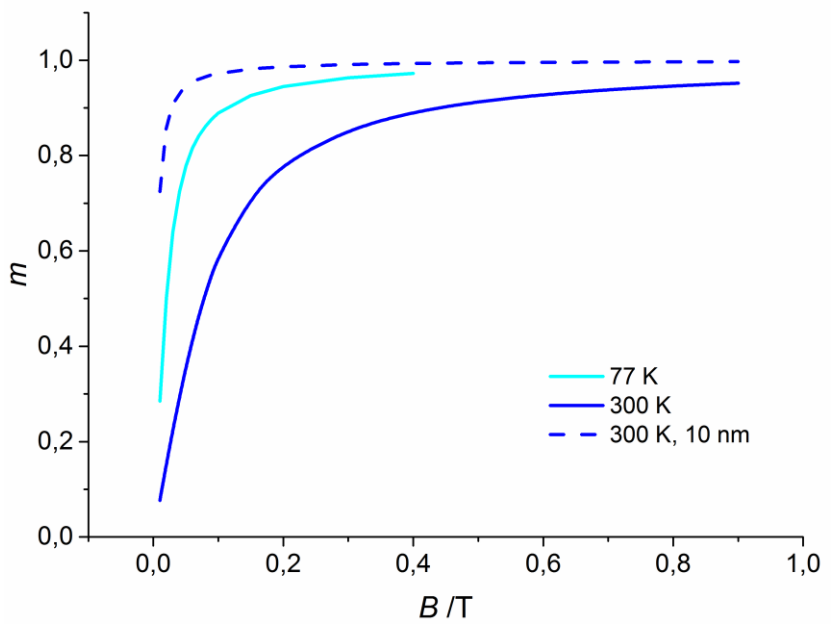

Figure 3. Magnetic flux dependence of the reduced magnetization of Fe NPs with a d = 4 nm. The curve for d = 10 nm at 300 K is shown for comparison.

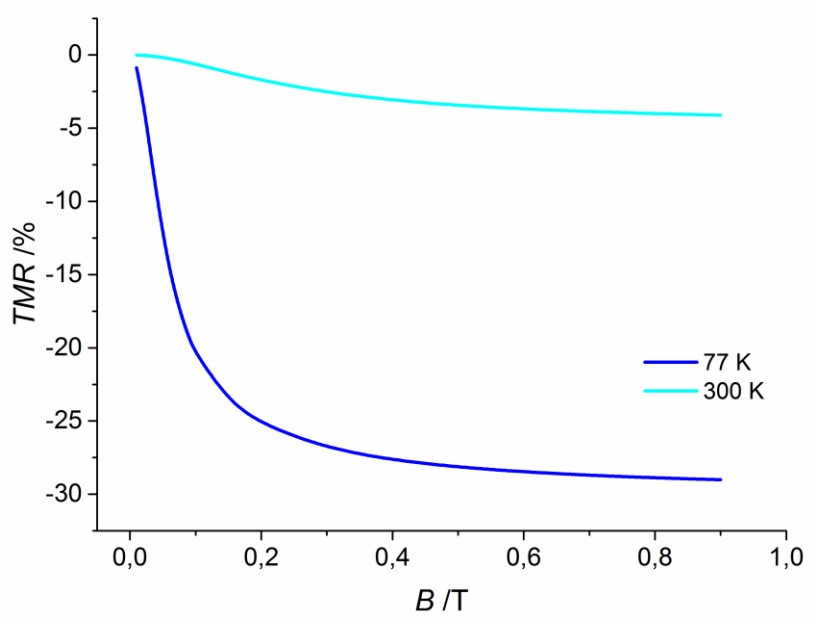

Figure 4. Magnetic flux dependence of the TMR of SPM SFMO NPs with d = 10 nm.

Figure 3 depicts the field dependence of NPs with a diameter of 4 nm. Liquid nitrogen is suitable as a coolant for magnetic sensors to provide the condition of a constant temperature and to avoid thermal fluctuations. For this reason, data calculated for 77 K is shown in the following for comparison.

Figure 4 illustrates the TMR for SPM SFMO NPs of about 10 nm diameter calculated by means of equations (5), (9) and (17). Here, a temperature dependence appears due to the temperature dependencies of spin polarization and magnetization. The temperature coefficient of the TMR (TC_{TMR}) amounts to $-8.7\cdot10^{-3}$ and $-2.1\cdot10^{-2}$ K^{-1} at 0.1 T and 77 and 300 K, respectively. SPM SFMO NPs are suitable for application as a magnetic field sensor at liquid nitrogen temperatures in the magnetic field range up to about 100 mT.

Now we turn to a special tunnelling effect in granular systems at low temperatures. We start with the resistance in granular systems – equation (1) – and the corresponding TMT – equation (9). In the granular systems with a broad distribution in granule size, it is highly probable that large granules are well separated from each other due to their low number density (that is, the larger the granule size is, the more separated the granules are). As a result, a number of smaller granules exist separating the large ones. Here, the ordinary tunnelling of an electron from the large granule to the small one increases the charging energy E_c, cf. equation (3), and suppresses tunnelling by the Coulomb blockade at low temperatures. In this case, higher-order tunnelling comes into play, i.e., the dominant contribution to the tunnelling current now comes from higher-order processes of spin-dependent tunnelling where the carrier is transferred from the charged large granule to the neighbouring neutral large granule through an array of small granules, using co-tunnelling of (p+1) electrons. The TMR is then given by [39]

$$TMR = \frac{1}{(1+m^2P^2)^{1+p^*}} - 1, \quad p^* = \frac{p^*(0)}{\sqrt{T}}, \qquad (18)$$

where $p^*(0)$ is a fitting parameter $p^*(0) > 2$ which is determined by the maximum of the distribution of conduction paths $f(p)$.

Figure 5 shows the calculated TMR of Co NPs due to higher order tunnelling – equation (18) – compared with the TMR without higher order tunnelling – equations (5) (9) and (17) – and experimental data attributed to higher order tunnelling in granular Co-Al_2O_3 [40]. Similar effects occur in granular zinc ferrite-ferric oxide [41]. High order tunnelling does not occur at room temperature since here p^* tends to zero.

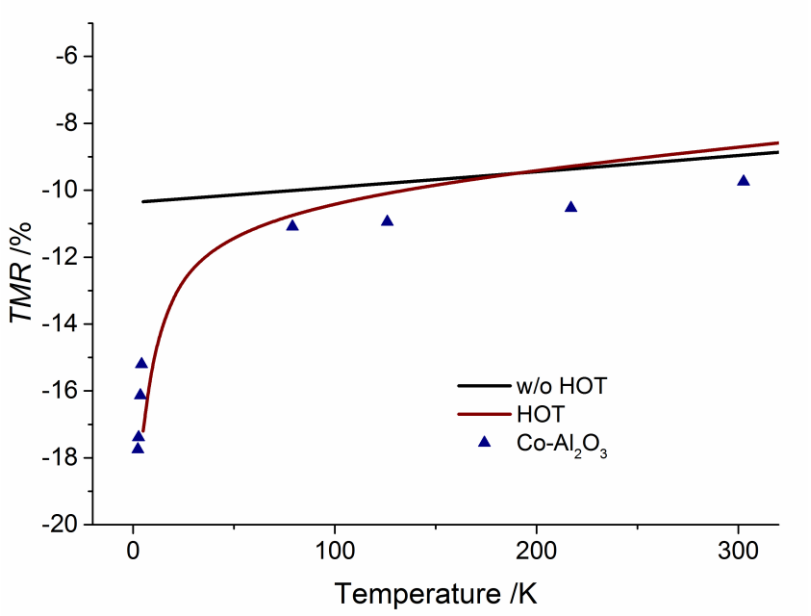

Figure 5. Calculated TMR of Co NPs due to higher order tunnelling compared with the TMR without higher order tunnelling and experimental data of granular Co with d = 2-3 nm interconnected by a 1 nm thick Al_2O_3 barrier [40].

The magnetic field sensibility of a sensor is the derivative of the sensor signal by the magnetic flux density. When interparticle interactions are non-negligible, the magnetic behaviour becomes more complicated requiring a more complex theoretical treatment. Moreover, the interaction energy depends on the particular arrangement (volume, topology) of the NPs. On the other hand, the NPs of granular network are interconnected by insulating barriers. In this case, exchange interaction between spherical particles is negligible and only the magnetic-dipole interaction is significant. For sake of simplicity, we consider NPs as a magnetic dipole in its centre. Then adjacent particles influence each other via their dipolar coupling. Strong interactions will cause agglomerations of SPM NPs leading to hysteretic behaviour. Following the $1/r^3$-decay of the dipole field, the cut-off radius of dipolar interaction amounts to about five times the average SPM NP radius [42]. Spin dependent tunnelling occurs though thin enough barriers – in the order of 1 to 3 nm – where direct tunnelling occurs which is not disturbed by localized states in the thin barrier film. Here, magnetic coupling increases the stiffness magnetic behaviour lowering the response to an external magnetic field.

Early theoretical models of weak coupling in the presence of an interaction field in spin-glasses [43] and of dipolar interaction of two magnetic particles taking into account uniaxial magnetic anisotropy [44] predicted a decrease of T_B – equation (12) – with increasing magnetic interaction. Contrarily, Monte Carlo simulations studying dipolar interaction and polydispersity of single-domain ultrafine FM particles revealed an increase of T_B with increasing strength of interaction [45]. However, due to the onset of ordering at temperatures in the order of T_B, changes of T_B obtained magnetization measurements will be small. Thus, an upper limit of the magnetic field sensibility was calculated considering noninteracting SPM NPs. This yields

$$\frac{d(TMR)}{dB} = -\frac{2P^2L'(\zeta B)}{[1+P^2L(\zeta B)^2]^2} = -\frac{2P^2\zeta\cdot\left[\frac{1}{(\zeta B)^2}-\frac{1}{sinh^2(\zeta B)}\right]}{\left\{1+P^2\left[coth(\zeta B)-\frac{1}{\zeta B}\right]^2\right\}^2}, \quad (19)$$

where $L(\zeta B)$ is the Langevin function given in equation (17).

Figure 6 illustrates the magnetic field sensitivity of noninteracting, SPM Co NPs calculated using equation (5) and (17). A constant value is obtained

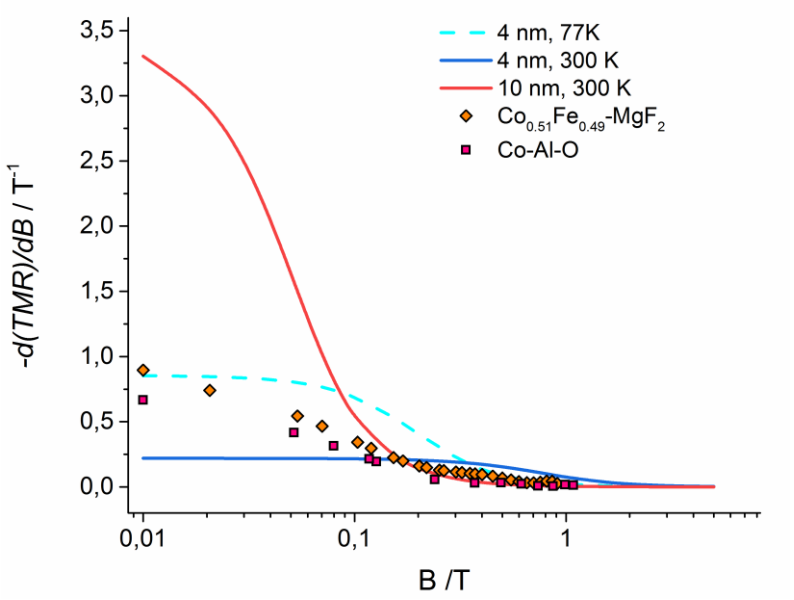

Figure 6. Upper limit of the magnetic field sensitivity of the TMR of SPM Co NPs with a diameter of 4 nm at 77 and 300 K and 10 nm at 300 K, respectively, compared with the field sensitivity derived from experimental data values of Co-Al-O [5] and $Co_{0.51}Fe_{0.49}$-MgF_2 [46] at 300K.

at low fields of practical interest. TC_{TMR} value without higher order tunnelling is about $-2.14 \cdot 10^{-4}$ K^{-1} at low temperatures while it increases to about $-3 \cdot 10^{-2}$ K^{-1} at 4 K with higher order tunnelling (cf. Figure 5). Note that cooled to 77 K sensors possess a higher sensitivity.

2.3. Granular networks of ferromagnetic nanoparticles

Up to now, there is no satisfactory analytical expression for the relative magnetization $m(T)$, i.e. the spontaneous magnetization M scaled to the saturation magnetization M_S at low temperatures, except for the two limiting cases, small temperatures $T \to 0$ and temperatures when approaching the Curie temperature $T \to T_C$ [47]. For sake of simplification, we make use of the simulation of the temperature dependent magnetization by Monte Carlo methods and Landau–Lifshitz–Gilbert atomistic spin models, equation (16) [35]. To calculate the temperature dependence of the reduced magnetization, we have used an approximation of m^2 known for Ni near Curie temperature [48] and made a series expansion [25]

$$m^2(T) = \sum_i a_i \left(1 - \frac{T}{T_C}\right)^i, \qquad (20)$$

The magnetic flux density dependence of the reduced magnetization was modelled by means of a traditional analysis of the approach of magnetization to saturation [49,50]

$$m(B) = 1 - \sum_i \left(\frac{b_{i/2}}{B}\right)^{i/2}, \qquad (21)$$

Table 1. Coefficients of the series expansion, equation (20) [25].

Parameter	Value
a_1	2.0
a_2	-2.3
a_3	2.6
a_4	-1.3

Table 2. Coefficients of the series expansion, equation (21) [25].

Parameter	Value, mT
$b_{1/2}$	7.4
b_1	16

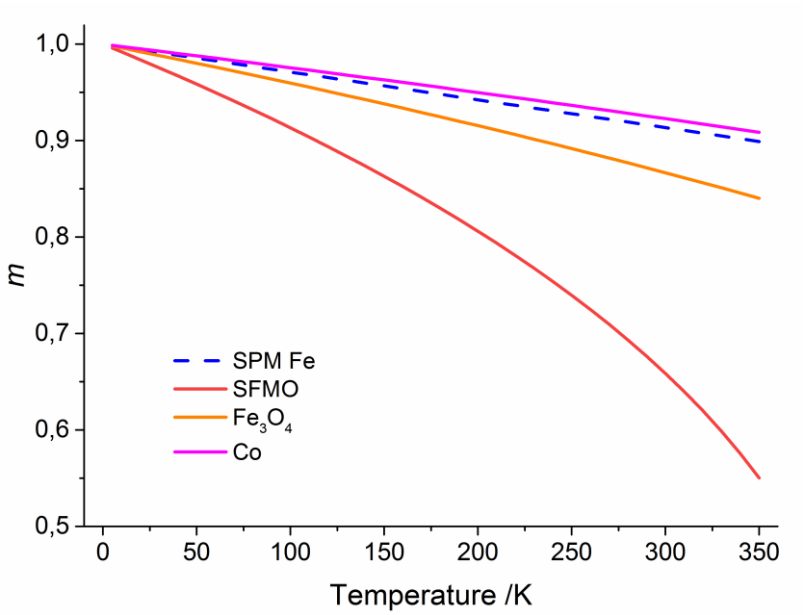

Figure 7. Comparison of the reduced magnetization m of FM SFMO, Fe_3O_4 and Co, equation (16), compared to the values of SPM Fe NPs with d = 10 nm at B = 0.5 T, equation (17).

Here, each of the lower terms of this expansion is associated with a certain source of magnetic inhomogeneities. i equals 1, 2, 3 for point, linear and layered sources, respectively [50]. On the other hand, the coefficient $b_{1/2}$ in SFMO ceramics was related also to the spin-glass-like behaviour of grain boundaries, the quadratic terms (i = 4) is related to the magnetocrystalline or shape anisotropy as well as to mechanical stress, the cubic term (i = 6) also includes magnetocrystalline anisotropy [25]. The corresponding coefficients for SFMO ceramics are shown in Table 1 and 2.

Figure 7 shows the comparison of reduced magnetization in the and FM and SPM state. In the

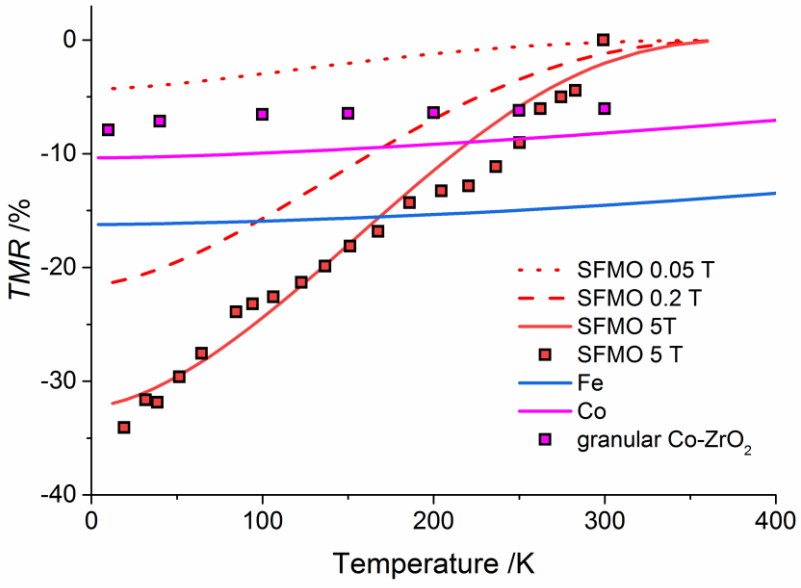

Figure 8. Calculated TMR of granular, ferrimagnetic SFMO in comparison with granular FM Fe, Co and experimental data of granular SPM Co-ZrO_2 thin films [53] as well as nanosized SFMO-$SrMoO_4$ core-shell structures fabricated by the citrate-gel technique [54].

.

first case, examples are SFMO, Fe_3O_4 and Co, while in the second case SPM Fe NPs at 0.5 T were considered. High values of the reduced magnetization at room temperature are obtained for high Curie temperatures.

Figure 8 shows the calculated TMR of granular, FM SFMO with the magnetic flux as parameter. The spin polarization at a given temperature was estimated by equation (5) and the reduced saturated magnetization by means of equation (20). Note that at lower magnetic fluxes, the magnetization is lower than the saturated one. For comparison, we consider Fe and Co, where a phenomenological model of the temperature dependence of *m* [51],

$$m = \left[1 - \left(\frac{T}{T_C}\right)^p\right]^\beta , \qquad (22)$$

was applied. The corresponding fitting parameters *p* and β are compiled in table 3. Also shown is a comparison with experimental data of SPM Co-ZrO_2 granular structures [52].

Due to a small TMR, SFMO is not applicable in magnetic sensors near room temperature. Co and Fe provide suitable values. The temperature dependence of the TMR of both Fe and Co are weak due to a weak temperature dependence of spin polarization. The TC_{TMR} values of Co and Fe increase with temperature reaching $-6.5\cdot10^{-4}$ and $-3.2\cdot10^{-4}$ K^{-1} at room temperature, respectively.

The magnetic field sensitivity of granular FM materials is given by

$$\frac{d(TMR)}{dB} = -\frac{2P^2\frac{dm(B)}{dB}\cdot m(B)\cdot m^2(T)}{\left[1+P^2m^2(T)\cdot m^2(B)\right]^2} , \qquad (23)$$

Figure 9 illustrate the calculation of the magnetic field sensitivity of granular FM Fe, Co and SFMO using equations (5), (21) and (23). Note that the curves in figure 9 depend significantly on the chosen model of *m*. For instance, the coefficients of SFMO in equation (21) are highly dependent on synthesis condition since they are determined by magnetic inhomogeneities.

Table 3. Parameters of equation (22) [51].

Compound	*p*	β
Fe	2.876	0.339
Co	2.369	0.34

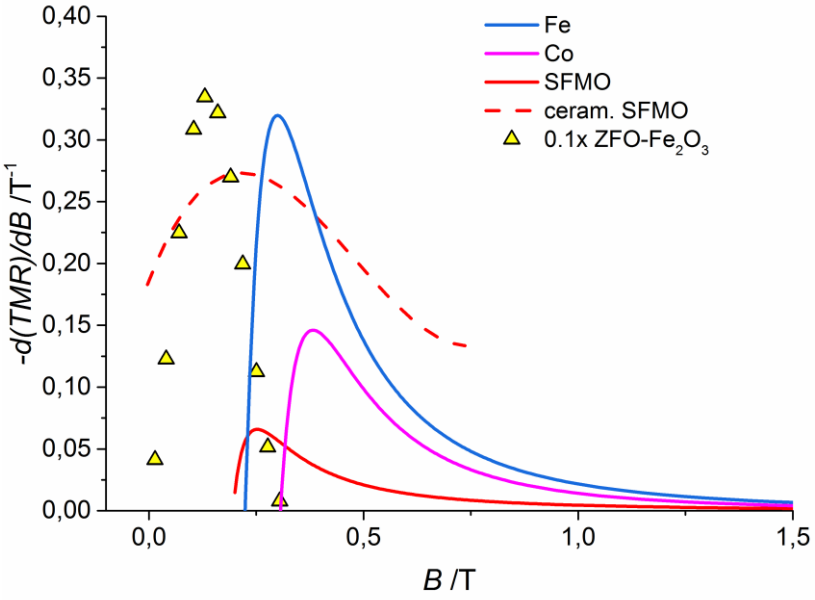

Figure 9. Magnetic field sensitivity of the TMR of FM Fe, Co and SFMO NPs at 300 K, respectively, in comparison with experimental data of ceramic SFMO annealed in reducing atmosphere at 10 K [54] and $Zn_{0.41}Fe_{2.59}O_4$-α-Fe_2O_3 core shell structure (multiplied by 0.1) with a size of about 160 nm at 300 K [41].

.

3. CONCLUSIONS

Granular, SPM materials show a higher magnetic field sensitivity than ferromagnetic ones. Also, they show a lower TC_{TMR}. Owing to their small magnetic response a higher temperature, SPM FM oxides are not suitable for application at room temperature. FM nanoparticles possess a high field sensitivity only in a small region of 0.1 to 0.5 T.

ACKNOWLEDGMENTS

This work was developed within the scope of the European project H2020-MSCA-RISE-2017-778308–SPINMULTIFILM.

REFERENCES

[1] J. Duran, *Sands, Powders, and Grains: An Introduction to the Physics of Granular Materials*, Springer Inc., New York, (1999).
[2] J. I. Gittleman, Y. Goldstein, and S. Bozowski, *Phys. Rev. B*, **5**, 3609 (1972).
[3] P. M. Tedrow and R. Meservey, *Phys. Rev. B*, **7**, 318 (1973).
[4] H. Karamon, T. Masumoto and Y. Makino, *J. Appl. Phys*. **57**, 3527 (1985).
[5] H. Fujimori, S. Mitani, and S. Ohnuma, *Mater. Sci. Eng. B*, **31**, 219 (1995).
[6] A. Milner, A. Gerber, B. Groisman, M. Karpovsky, and A. Gladkikh, *Phys. Rev. Lett*. **76**, 475 (1996).
[7] N. Kobayashi, S. Ohnuma, T. Masumoto, S. Mitani, and H. Fujimori, *J. Magn. Soc. Jpn* **21**, 461 (1997).
[8] H. Fujimori, S. Mitani, and S. Ohnuma, *J. Magn. Magn. Mater*. **156**, 311 (1996).
[9] Y. H. Huang, J. H. Hsu, and J. W. Chen, *IEEE Trans. Magn*. **33**, 3556 (1997).
[10] S. Mitani, Y. Shintani, S. Ohnuma, and H. Fujimori, *J. Magn. Soc. Jpn*. **21**, 465 (1997).
[11] S. Honda, T. Okada, and M. Nawate, *J. Magn. Magn. Mater*. **165**, 153 (1997).
[12] S. Honda, T. Okada, M. Nawate, and M. Tokumoto, *Phys. Rev. B* **56**, 14566 (1997).
[13] B. Zhao and X. Yan, *Physica A* **241**, 367 (1997).
[14] Y. Hayakawa, N. Hasegawa, A. Makino, S. Mitani, and H. Fujimori, *J. Magn. Magn. Mater*. **154**, 175 (1996).
[15] T. Furubayashi and I. Nakatani, *J. Appl. Phys*. **79**, 6258 (1996).
[16] N. Kobayashi, S. Ohnuma, T. Masumoto and H. Fujimori, *J. Appl. Phys*. **90**, 4159 (2001).
[17] S. Ohnuma, M. Ohnuma, H. Fujimori, and T. Masumoto, *J. Magn. Magn. Mater*. **310**, 2503 (2007).
[18] N. Kobayashi, K. Ikeda, Bo Gu, S. Takahashi, H. Masumoto, and S. Maekawa, *Sci. Rep*. 8, 4978 (2018).
[19] J. S. Helman and B. Abeles, *Phys. Rev. Lett*. **37**, 1429 (1976).
[20] B. Abeles , Ping Sheng , M.D. Coutts and Y. Arie, *Adv. Physics* **24**, 407 (1975).
[21] J. G. Simmons, *J. Appl. Phys*. **34**, 1793 (1963).
[22] J. Inoue and S. Maekawa, *Phys. Rev. B* **53**, R11927 (1996).
[23] G. Suchaneck, *Electron. Mater*. **3**, 227 (2022).
[24] L. López-Mir, C. Frontera, H. Aramberri, K. Bouzehouane, J. Cisneros-Fernández, B. Bozzo, L. Balcells, and B. Martínez, *Sci. Rep*. **8**, 861 (2018).
[25] E. Artiukh and G. Suchaneck, *Open Ceram*. **7**, 100171 (2021).
[26] D. Serrate, J. M. De Teresa, P. A. Algarabel, M. R. Ibarra, and J. Galibert, *Phys. Rev. B* **71**, 104409 (2005).
[27] L. Néel, *Ann. Geophys*. **5**, 99 (1949).
[28] W. F. Brown, *Phys. Rev*. **130**, 1677 (1963).
[29] B. D. Cullity and C.D. Graham, *Introduction to Magnetic Materials*, p. 384, John Wiley & Sons Inc., Hoboken (NJ) (2008).
[30] C. Zener, *Phys. Rev*. **96**, 1335 (1954).
[31] C. L. Chien, *J. Appl. Phys*. **69**, 5267(1991).
[32] C. P. Bean and J. D. Livingston, *J. Appl. Phys*. **30**, S120 (1959).
[33] E. R. Callen and H. B. Callen, *J. Phys. Chem. Solids* **27**, 1271 (1966).
[34] S. Chikazumi, *Physics of Ferromagnetism, 2nd ed.*, p. 273, Oxford University Press, Oxford, (1997).
[35] R. F. L. Evans, W. J. Fan, P. Chureemart, T. A. Ostler, M. O. A. Ellis, and R. W. Chantrell, *J. Phys.: Condens. Matter* **26**, 103202 (2014).
[36] G. Suchaneck, N. Kalanda, M. Yarmolich, E. Artiukh, G. Gerlach and N. A. Sobolev, *Electron. Mater*. **3**, 82 (2022).
[37] F. Ibrahim, A. Hallal, A. Kalitsov, D. Stewart, B. Dieny, and M. Chshiev, *Phys. Rev. Appl*. **17**, 054041 (2022).
[38] X. Batlle, A. Labarta, *J. Phys. D: Appl. Phys*. **35**, R15 (2002).
[39] S. Mitani, S. Takahashi, K. Takanashi, K. Yakushiji, S. Maekawa, and H. Fujimori, *Phys. Rev. Lett*. **81**, 2779 (1998).
[40] S. Mitani, H. Fujimori, K. Takanashi, K. Yakushiji, J.-G. Ha, S. Takahashi, S. Maekawa, S. Ohnuma, N. Kobayashi, T. Masumoto, M. Ohnuma and K. Hono, *J. Magn. Magn. Mater*. **198-199**, 179 (1999).
[41] P. Chen, D.Y. Xing, Y.W. Du, J. M. Zhu, and D. Feng, *Phys. Rev. Lett*. **87**, 107202 (2001).
[42] V. Schaller, G. Wahnström, A. Sanz-Velasco, P. Enoksson, P. J. Johansson, *J. Magn. Magn. Mater*. **321**, 1400 (2009).
[43] S. Shtrikman and E. P. Wohlfarth, *Phys. Lett. A* **85**, 467 (1981).
[44] J L Dormann, L Bessais and D Fiorani, *J. Phys. C: Solid State Phys*. **21**, 2015 (1988).
[45] J. García-Otero, M. Porto, J. Rivas, and A. Bunde, *Phys. Rev. Lett*. **84**, 167 (2000).
[46] N. Kobayashi, S. Ohnuma, T. Masumoto and H. Fujimori, *J. Appl. Phys*. **90**, 4159 (2001).
[47] G. Suchaneck, *Mod. Electron. Mater*. **7**, 85 (2021).
[48] A. Arrott and J.E. Noakes, *Phys. Rev. Lett*. **19**, 786 (1967).
[49] W. F. Brown, Phys. Rev. **58**, 736 (1940).
[50] W. F. Brown, *Micromagnetics, 1st ed.*, J. Wiley, New York (1963).
[51] R. F. L. Evans, U. Atxitia, and R. W. Chantrell, *Phys. Rev. B* **91**, 144425 (2205).
[52] B. J. Hattink, M. García del Muro, Z. Konstantinović, X. Batlle, and A. Labarta, *Phys. Rev. B* 73, 045418 (2006).
[53] N. Kalanda, S. Demyanov, M. Krupa, and S. M. Konoplyuk, *Phys. Status Solidi* **B259**, 2200021 (2022).
[54] J.-F. Wang, Z. Li, X.-J. Xu, Z.-B. Gu, G.-L. Yuan, and S.-T. Zhang, *J. Am. Ceram. Soc*., **97**, 1137 (2014).